Ion Cyclotron Heating in an Electrodeless Water Vapor Thruster

IEPC-2017-468

Presented at the 35th International Electric Propulsion Conference
Georgia Institute of Technology – Atlanta, Georgia – USA
October 8–12, 2017

Elaine M. Petro* and Raymond J. Sedwick†
University of Maryland, College Park, Maryland, 20742, USA

Abstract: An analysis is performed to assess the efficacy of ion cyclotron heating (ICH) for a small-scale electrodeless thruster with water vapor as its propellant. Ion heating and conversion of perpendicular to parallel energy are captured using 3D particle trajectory simulations. Calculations are performed to couple the magnetic field strength, device radius, and antenna length. Analysis of a 10 centimeter diameter ICH stage is presented.

Nomenclature

B	= magnetic field strength
d	= distance between parallel plate electrodes
ϵ	= dielectric constant
ε_{ICH}	= ion cyclotron energy
E	= electric field strength
I	= current
I_{sp}	= specific impulse
g	= acceleration due to gravity
m	= mass
μ_0	= permeability of free space
N	= number of cyclotron oscillations
n_{turns}	= numbers of turns of wire
n_e	= electron density
ϕ_0	= electric field phase
q	= plasma shielding parameter
r	= radius
R_m	= magnetic field (mirror) ratio
t	= time
t_{wire}	= thickness of wire
T_e	= electron temperature
T_i	= ion temperature
V_0	= potential difference
ω_{ce}	= electron cyclotron frequency
ω_{ci}	= ion cyclotron frequency
ω_{pe}	= electron plasma frequency

*Graduate Research Assistant, Department of Aerospace Engineering, epetro@terpmail.umd.edu
†Associate Professor, Department of Aerospace Engineering, sedwick@umd.edu

I. Introduction

Electrodeless plasma thrusters offer the potential for high specific impulse propulsion without the need for life-limiting cathodes and accelerating grids. The absence of metal electrodes in the plasma environment allows for a wide range of potential propellants, including oxygen-containing molecular gases. There has been extensive research on the performance of these systems in a single-stage configuration both with traditional noble gases[1–3] and with molecular gas[4–7] propellants. Despite the additional loss mechanisms introduced by molecular propellants, specific impulses in excess of 1000 seconds have been measured and thrust efficiencies comparable with noble gas operation are predicted. However these theoretical calculations predict a maximum thrust efficiency of approximately 30% in a traditional configuration, regardless of propellant type, and not far above 50% with an upstream magnetic mirror added to reduce wall losses.[1,7,8]

While the thrust efficiencies of the single-stage system are greatly improved by the addition of an upstream magnetic mirror, the above (idealized) results are still below many state-of-the-art Hall thrusters and ion engines.[9] Thus, the performance gains that can be realized through the addition of an acceleration stage are investigated. An electrodeless acceleration stage is preferred due to the grid degradation that would be expected in a oxygen-containing plasma environment for propellants such as water vapor. Water vapor is the propellant of interest for the present analysis due to its prevalence throughout the solar system and ease of storability. The acceleration mechanism investigated here is ion cyclotron heating (ICH).

The application of ion cyclotron heating to plasma propulsion has been demonstrated in the VASIMR system[10] to effectively increase the thrust energy of the exhaust by resonantly heating the ions. The ions gain a large rotational energy, which is converted to translational energy due to conservation of the magnetic moment as the plasna expands through a diverging magnetic nozzle. The VASIMR group has demonstrated the efficacy of ion cyclotron heating for a range of propellants (H_2, D_2, Ar) and have demonstrated thrust efficiency in excess of 70% at high power levels (200 kW).[11] The goal of this analysis is to assess the scalability of this process for a small scale, moderate power water-propelled thruster.

The present work builds on a preliminary zero-D analysis[12] that predicted the overall thrust efficiency for a range of ICH energies and confining magnetic field strengths, for both argon and water propellants. In this preliminary analysis, power fluxes upstream, to the lateral walls, and out the thruster exit were compared to the exhaust beam power (diagram in Fig. 1). This analysis relied on simplifying assumptions such as monoenergetic ions, radially uniform densities and velocities, and 100% efficient ICH energy deposition and conversion. Despite its limited fidelity, the zero-D model revealed constraints on ICH operating regimes and an upper limit on energy deposition for a given axial magnetic field strength and chamber radius. This analysis revealed that there should exist an optimum downstream mirror ratio ($R_{m,2}$) for a given upstream mirror ratio ($R_{m,1}$), specific impulse, and electron temperature that maximizes efficiency. If the mirror ratios are fixed (e.g. $R_{m,1} = \alpha R_{m,2}$), there should exist an ICH energy (ε_{ICH}) that maximizes thrust efficiency.

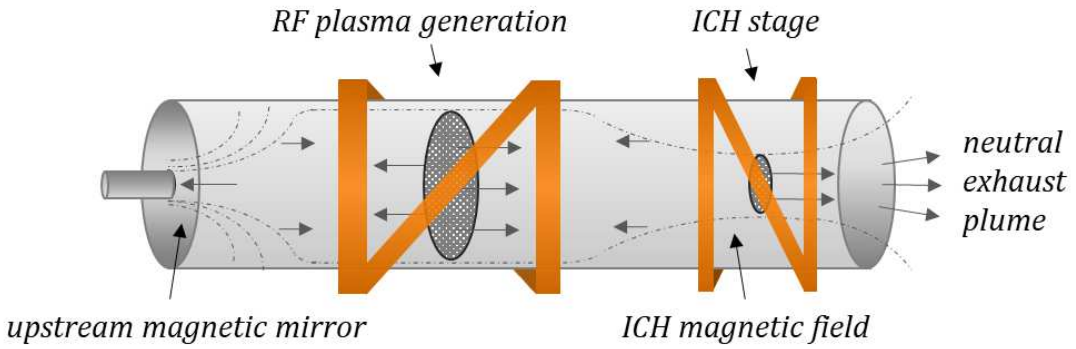

Figure 1. Diagram of charged particle fluxes in a two-stage electrodeless plasma thruster employed in a thrust efficiency analysis.[12]

The present analysis seeks to better capture the physics of the second stage heating and acceleration through 3D particle trajectory modeling. The system parameters (magnetic mirror ratios, ICH energy) from the zero-D model are used as inputs in the present analysis and implications for heating efficiency are predicted. In future work, the particle trajectory model presented here will be used to narrow down the design space for efficient implementation of ion cyclotron heating at a small scale. Once a design point has

been selected, the system will be modeled using particle-in-cell methods to capture interactions between plasma particles and external electric and magnetic fields.

II. Methodology

II.A. Magnetic Field Model

A strong axial magnetic field is required for ion heating and confinement. The 3D components of the magnetic field are calculated in the simulation domain using a Biot-Savart solver implemented in MATLAB. Azimuthal current densities and wire dimensions are specified and the Biot-Savart law is numerically integrated over discretized current segments to calculate $\vec{B}(\vec{x})$.

The centerline axial magnetic field strength in the heating region is constrained by:

1. Specified strength ratios between the ICH field and the upstream mirror field identified in the zero-D analysis
2. Properties of state-of-the-art high temperature superconducting (HTS) tape

It is important that the magnetic field at the upstream wall be higher than the magnetic field in the ICH system so that the plasma preferentially flows downstream toward the exit. In the previous analysis, several magnetic field strength ratios were evaluated. Each ratio is defined with respect to the magnetic field in the plasma generation region, as defined in Fig. 2. For the 10 cm radius case previously considered, thrust efficiency over 80% was predicted with the magnetic field ratios $R_{m,1} = 20$ and $R_{m,2} = 10$. Thus these ratios are chosen to constrain the ICH stage magnetic field strength for the present analysis.

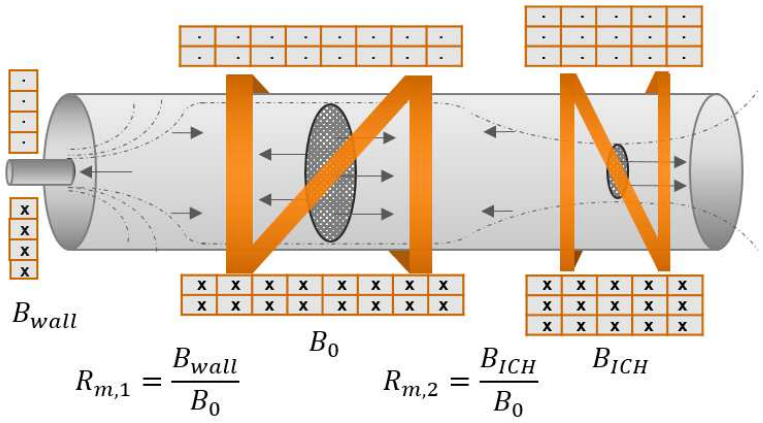

Figure 2. This diagram shows the three distinct magnetic field regions and defines the mirror ratios, $R_{m,1}$ and $R_{m,2}$.

The magnetic field, B_{wall}, that creates the upstream magnetic mirror is chosen to be the maximum field that can be created using currently available HTS tape.[13] It is assumed that the magnetic field is generated using a multi-turn current loop with the inner radius set equal to the minimum bend radius of the wire ($r_{min} = 5$ mm), carrying the maximum superconducting current at 77 K ($I = 300A$). This wire can be made in lengths up to 500 m,[14] thus the number of turns in the current loop is calculated under this constraint. The thickness, t_{wire}, of the wire is 0.1 mm.

The magnetic field on axis at the center of the current loop can be approximated using Eq. (1).

$$B_{center} \approx \frac{\mu_0 I}{2\bar{r}} \tag{1}$$

with $\bar{r} = (r_{min} + n_{turns}t/2)$.

The maximum magnetic field upstream is thus estimated to be **3.5 T**. Note that the actual field could be reduced from this value due to (1) the need to operate below the critical current to remain superconducting and (2) the effects of magnetic fields at the wire location on the critical current value.[15]

Using the mirror ratios defined above, we thus require a centerline magnetic field strength of approximately **1.75 T** in the ICH section. The ICH magnetic field should be constant under the antenna to

maintain resonance at the ion cyclotron frequency. Thus the field should be generated with an HTS solenoid or Helmholtz coils (the latter only if the device radius and antenna length are of comparable dimensions). The relationship between ICH field strength and antenna will be discussed in Section II.D.

Examples of both a solenoid and Helmholtz coil field for a 5 cm radius ICH chamber are shown in Fig. 3. It will be interesting in future analysis to compare the efficiency of both heating and magnetic nozzle expansion in these two magnetic field configurations.

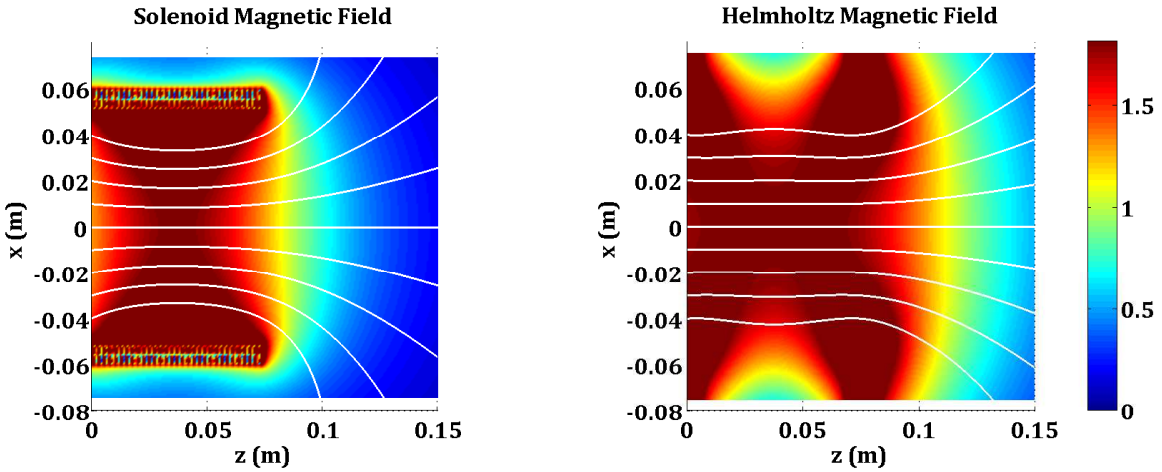

(a) Magnetic field generated by solenoid of 5 cm inner radius, 7.5 cm length, and 55 layers of wire carrying 300 A.

(b) Magnetic field generated by Helmholtz coils of 5 cm inner radius with 500 layers of wire carrying 300 A, located 7.5 cm apart.

Figure 3. Comparison of ICH magnetic fields generated by (a) solenoid and (b) Helmholtz coil configurations.

II.B. Electric Field Model

Despite the depiction of the ICH antenna in Figs. 1 and 2 as helical, the electric field implemented for these calculations is actually more simplified. A uniform, linearly polarized electric field is implemented for this analysis. The accelerating electric field is modeled as the 1D electric field between two parallel plates separated by a distance, $d \approx 2r$, with a potential difference, V_0, oscillating at the ion cyclotron frequency. For the selected magnetic field strength, the vacuum electromagnetic wavelength ($\frac{2\pi c}{\omega_{ci}}$) is 33 meters and thus much larger than the device radius. Additionally, assuming the strong magnetic field increases the skin depth beyond the size of the radius, a 1D, electrostatic approximation may be applied.[16]

Plasma shielding of the electric field is accounted for using the model developed by Matsuoka.[17] In this model, the plasma is separated into 3 regions with different dielectric properties, as depicted in Fig. 4. The dielectric constant of the bulk plasma is given by the perpendicular component of the cold plasma dielectric tensor, where ω_{pe} is the electron plasma frequency and ω_{ce} is the electron cyclotron frequency. Poisson's equation is solved across all three regions to find the electric field inside the plasma.

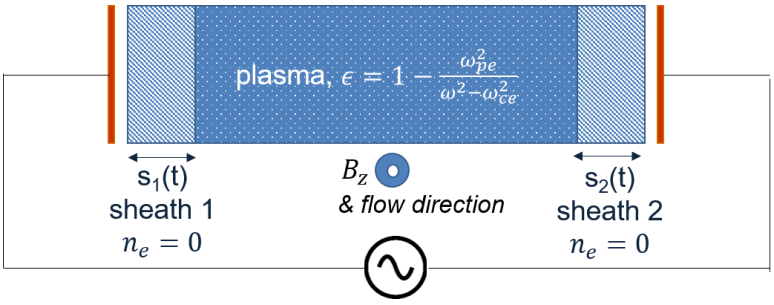

Figure 4. This diagram shows the three plasma regions between parallel plate electrodes.

The electric field inside the plasma can then be related to the vacuum electric field ($E_{vac} = V_0/d$) as given in Eq. (2), through the non-dimensional shielding parameter, q, which depends on the plasma and

electrode properties.

$$E_p = E_0 \left(\frac{2\sqrt{1+q} - 1}{q} \right) \tag{2}$$

When $q \ll 1$, the electric field within the plasma is indistinguishable from the vacuum field created by parallel plates. The shielding parameter is calculated for a range of parameters that could be expected in the ICH stage and the results are shown in Fig. 5. In the strong magnetic field case, the shielding parameter remains negligible for all plasma densities. Thus, according to this model, the parallel plate electric field should fully penetrate the plasma. The electric field in the region under the antenna is therefore modeled as a spatially uniform and sinusoidally time-varying field of arbitrary phase, ϕ_0, between parallel plates located at the radial edges of the plasma (Eq. (3)).

$$\vec{E}(\vec{x}, t) = \frac{V_0}{d} cos(\omega_{ci} t + \phi_0)\hat{y} \tag{3}$$

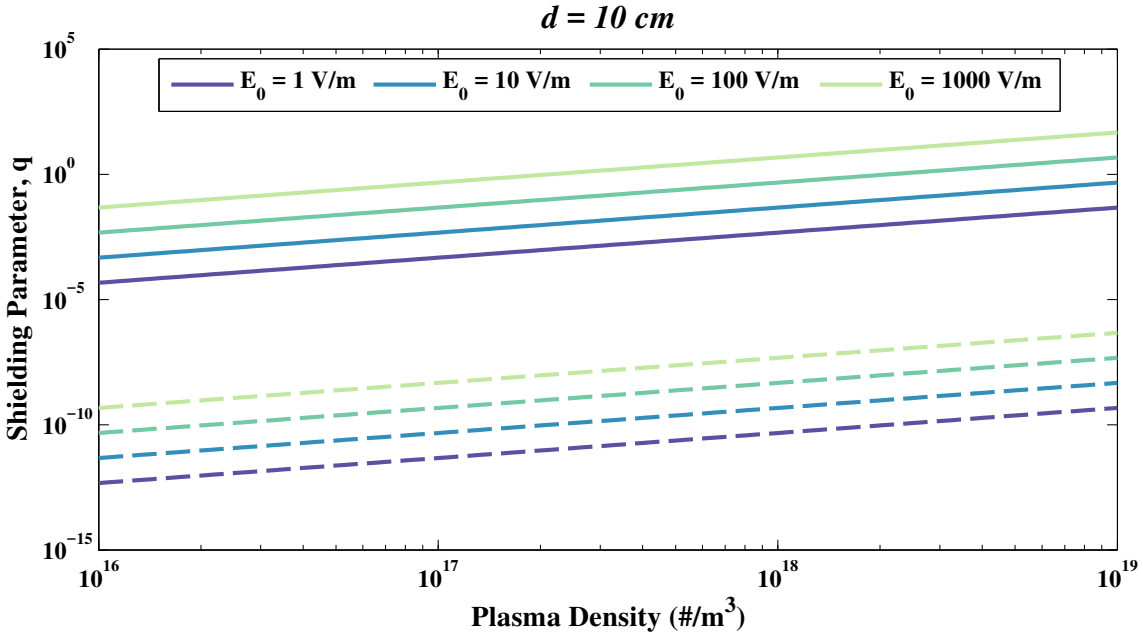

Figure 5. Shielding parameter for magnetic field strengths of 100 Gauss (solid lines) and 1 Tesla (dotted lines) for a range of electric field strengths and plasma densities.

II.C. Particle Trajectory Model

The trajectories of individual test particles are calculated throughout the ICH heating and magnetic nozzle regions. The inputs to the trajectory model are the particle's initial conditions $(\vec{x_0}, \vec{v_0})$, the external electric field in the solution domain, and the magnetic field profile. The particle trajectory is calculated via numerical integration using the Boris Method.[18] In this case, the only forces that act on the particles once they enter the ICH stage are due to the applied electric and magnetic fields. No forces due to internal plasma fields nor pressure gradients are captured.

II.D. Simulation Constraints and Input Parameters

The strength of the electric field, magnetic field, and the antenna length are coupled through the desired performance parameters. The process by which each parameter is determined for the simulation is outlined below:

1. **Performance Parameters:** The desired specific impulse, I_{sp} and device radius, r, are specified. Water ions (H_2O^+) are assumed in this analysis as they are expected to be the predominant ion generated in the upstream discharge.[7] The desired final kinetic energy is calculated from the I_{sp}:

$$KE_f = \frac{1}{2} m_i I_{sp}^2 g^2 \tag{4}$$

2. **Antenna Length:** The antenna must have an axial extent that allows a plasma ion to complete several cyclotron revolutions as it passes through. As a starting point, ten revolutions are required. This allows for any initial phase difference between the incoming ion velocity vector and the electric field to be corrected within the first few cycles and then several cycles of maximally efficient heating when aligned. This parameter may be adjusted and optimized through future analyses. It is assumed that the ions travel across the constant magnetic field region (representing the throat of a magnetic nozzle) at their acoustic speed ($v_{0||} = \sqrt{\frac{eT_e}{m_i}}$).

   The antenna length, L_{ant}, is thus given by:

$$L_{ant} = 10 \left(\frac{2\pi}{\omega_{ci}} \right) v_{0||} \tag{5}$$

   This is also the length over which the magnetic field should be approximately constant and thus determines the solenoid length (or Helmholtz coil sizing). For this analysis, an electron temperature of 5 eV is assumed, which leads to an antenna length of **3.4 cm**.

3. **Electric Field:** The strength of the electric field required to heat the particles can be related to the the desired final kinetic energy, the number of cycles under the antenna, and the antenna frequency. A simple expression for the electric field can be derived for the case where the particle and electric field are in phase at the start of the antenna region:

$$\varepsilon_{ICH} = \frac{1}{2} m_i \left(v_{f\perp}^2 - v_{0\perp}^2 \right) = eE_p \left(\frac{2\pi}{\omega_{ci}} \right) \left(\frac{v_{f\perp} - v_{0\perp}}{N} \right) \int_0^N cos^2(2\pi N') N' dN' \tag{6}$$

   where N is the number of revolutions completed by the particle while transiting the heating region. Note that for the conditions analyzed in this study, phase-matching is typically achieved within two periods of oscillation.

   When $v_{f\perp} \gg v_{0\perp}, v_{0||}$, Eq. 6 can be simplified to solve for E_0 as a function of the desired Isp ($v_{f\perp} \approx I_{sp} g$). Recall that in this case, $E_0 = E_p = \frac{V_0}{d}$.

$$E_0 \approx \frac{B_{ICH} I_{sp} g}{4\pi} \left(\frac{N}{\alpha(N)} \right) \tag{7}$$

   with $\alpha(N) = \int_0^N cos^2(2\pi N') N' dN'$.

   A plot of the resulting specific impulse as a function of the electric field across the plates is shown in Fig. 6, for three different antenna sizes. The middle antenna length, 3.4 cm, corresponds to N = 10 cycles when the particle enters in phase with the electric field.

4. **Magnetic Field:** A time-invariant magnetic field that is approximately constant in the heating region can be generated using a solenoid or Helmholtz coils. The coil current, number of turns, and axial extent are specified and the 3D components of the magnetic field are calculated throughout the simulation domain. For the present analysis, the solenoid magnetic field shown in Fig. 3(a) is used.

5. **Particle Trajectory:** Initial conditions are specified for each particle at the beginning of the ICH region. The particles are assumed to have an initial perpendicular velocity, $v_{i\perp,0} = \sqrt{\frac{eT_{i,0}}{m_i}}$ where $T_{i,0} = 0.025$ eV. Cases are evaluated where the particle velocity is both in and out of phase with the electric field when entering the antenna region to assess the influence of phasing on heating efficiency. The particle trajectory is integrated out to 7.5 cm past the last magnetic field coil in these analyses, although the solution domain could be easily extended further.

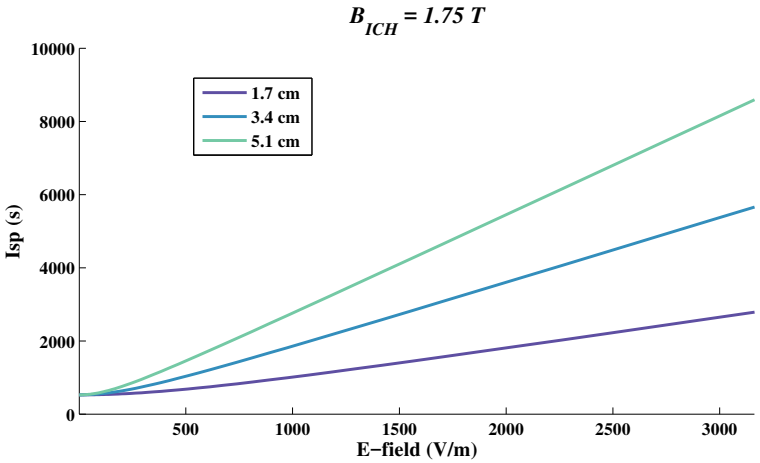

Figure 6. Specific impulse as a function of oscillating electric field strength for three different antenna lengths.

III. Results

The simulated particle trajectory is shown in Fig. 7 for the input parameters specified in Table 1. The evolution of the particle's perpendicular velocity as it traverses the ICH region is also shown in Fig. 8. The particles simulated in this case start approximately on axis (offset by the particle's initial Larmor radius).

Table 1. Simulation parameters: on-axis, in-phase

B_{ICH}	T_e	L_{ant}	$z_{0,ant}$	$Desired\ I_{sp}$	E_0	$\vec{x}_0$	$\vec{v}_0$
1.68 T	5 eV	3.4 cm	2.05 cm	5000 s	3000 V/m	(0, 56.8, 0) μm	(-365, 0, 5160) m/s

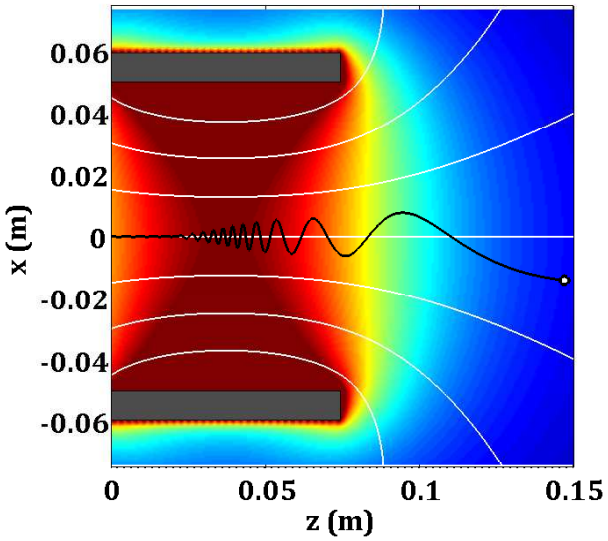

Figure 7. Trajectory traced out by a charged water ion with simulation parameters listed in Table 1. Magnetic field contour and streamlines are shown in the background.

A second particle is simulated for this case with initial conditions that are phase-shifted 180^o from the previous particle. The final increase in total kinetic energy for the in-phase particle differs from that of the out-of-phase particle by less than 0.1 %. Therefore we conclude that for these conditions, the effect of particle phasing is negligible.

At the final simulation time, the parallel velocity of the particle is 44,350 m/s. If the particle were able

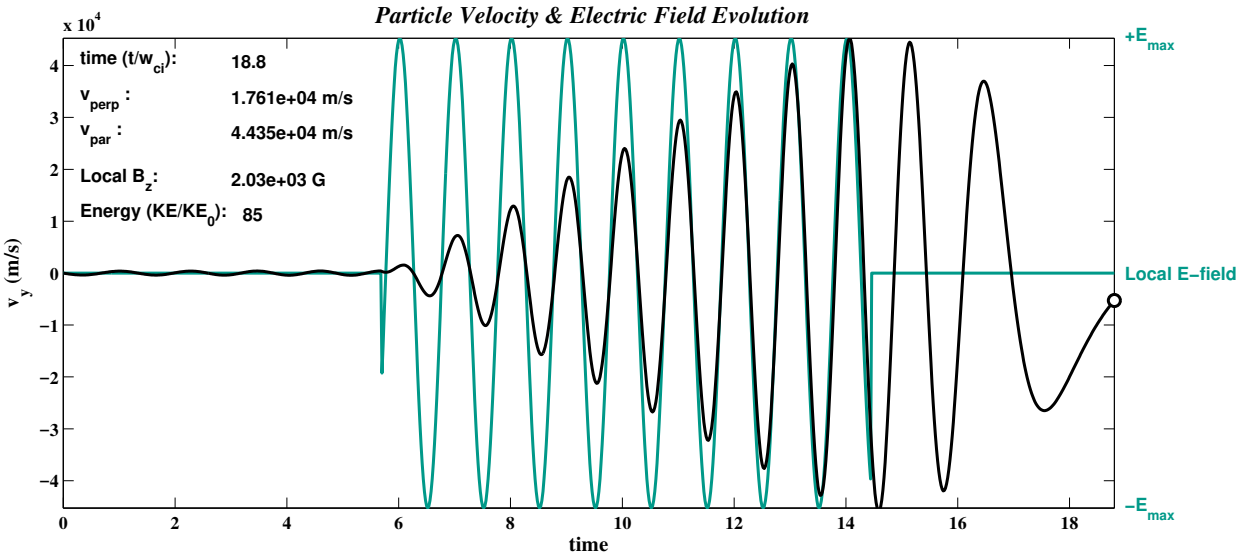

Figure 8. Plot of evolution of charged water ion velocity for simluation parameters listed in Table 1.

to follow the magnetic field line until all perpendicular kinetic energy could be converted to parallel energy, the particle Isp would be 4870 s. The Isp falls short of the 5000 s design point because of imperfect RF energy absorption.

The Larmor radius of the particle as a function of z-position is shown in Fig. 9. At the end of the simulated region, the magnetic field is still quite high (2030 Gauss) and the Larmor radius has grown to only 1.6 cm. Future analyses will include trajectory calculations for particles at the radial edges of the plasma to assess the effects of both wall losses and magnetic field divergence on efficiency.

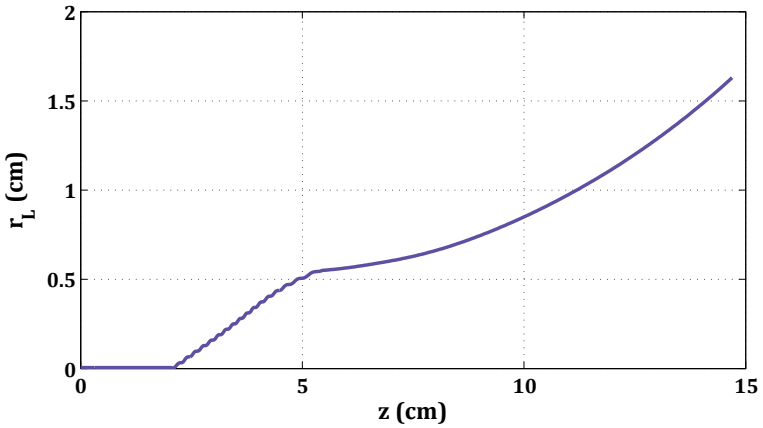

Figure 9. Evolution of the Larmor radius as the particle traverses the ICH stage into the magnetic nozzle region.

IV. Conclusions and Future Work

A tool has been developed to study the trajectories of plasma particles in the ion cyclotron resonance heating stage of an electrodeless plasma thruster. Externally applied electric and magnetic fields are specified in the simulation region. The position and velocity of the charged particle, a water ion in this case, is integrated across the simulation domain for a set of initial conditions. The kinetic energy absorption and conversion of perpendicular to parallel velocity are captured through these calculations.

A test case for a particle starting at the centerline of the thruster is presented. Future work will include expansion to particles at all starting radial locations. The results could be generalized to a thruster

configuration by incorporating common radial density distributions for electrodeless thrusters.

Further development of the model should take into account collisions between water ions and background plasma and neutral species. Trajectory modeling will be used to perform scaling studies, whereas more complex particle-in-cell or magnetohydrodynamic methods will be required to properly model electric field penetration and ion plume detachment for chosen designs.

Acknowledgments

This material is based upon work supported by the National Science Foundation Graduate Research Fellowship Program under Grant No. DGE 1322106. Additional support by the Amelia Earhart Fellowship through the Zonta Foundation and by the ARCS Fellowship is gratefully acknowledged.

References

[1] Ahedo, E. and Navarro-Cavalle, J., "Helicon Thruster Plasma Modeling: Two-Dimensional Fluid-dynamics and Propulsive Performances," *Physics of Plasmas*, Vol. 20, No. 4, 2013.

[2] Lafleur, T., "Helicon Plasma Thruster Discharge Model," *Physics of Plasmas*, Vol. 21, No. 4, 2014.

[3] Rafalskyi, D. and Aanesland, A., "Brief review on plasma propulsion with neutralizer-free systems," *Plasma Sources Science and Technology*, Vol. 25, No. 4, 2016, pp. 43001.

[4] Gilland, J. H. and Piefer, G., "Small Helicon Plasma Source Experiments," *40th AIAA/ASME/SAE/ASEE Joint Propulsion Conference and Exhibit*, No. 11-14 July, AIAA 2004-3939, Fort Lauderdale, FL, 2004.

[5] Charles, C., Boswell, R. W., Laine, R., and MacLellan, P., "An Experimental Investigation of Alternative Propellants for the Helicon Double Layer Thruster," *Journal of Physics D: Applied Physics*, Vol. 41, No. 17, 2008, pp. 175213.

[6] Bosi, F., Trezzolani, F., Lucca Fabris, A., Manente, M., Melazzi, D., and Pavarin, D., "Modelling and Optimization of Electrode-less Helicon Plasma Thruster with Different Propellants," *50th AIAA/ASME/SAE/ASEE Joint Propulsion Conference*, AIAA 2014-3404, Cleveland, OH, 2014.

[7] Petro, E. and Sedwick, R., "Effects of Water Vapor Propellant on Electrodeless Thruster Performance," *Journal of Propulsion and Power*, Vol. 0, No. 0, 2017.

[8] Vitucci, J. and Sedwick, R., "Development of a Superconducting Helicon Thruster," *48th AIAA/ASME/SAE/ASEE Joint Propulsion Conference & Exhibit*, AIAA 2012-3866, Atlanta, GA, 2012.

[9] Petro, E. M. and Sedwick, R. J., "Survey of Moderate-Power Electric Propulsion Systems," *Journal of Spacecraft and Rockets*, Vol. 54, No. 3, 2017, pp. 529–541.

[10] Bering, E. A., Chang-Diaz, F. R., Squire, J. P., Brukardt, M., Glover, T. W., Bengtson, R. D., Jacobson, V. T., McCaskill, G. E., and Cassady, L., "Electromagnetic Ion Cyclotron Resonance Heating in the VASIMR," *Advances in Space Research*, Vol. 42, No. 1, 2008, pp. 192–205.

[11] Longmier, B. W., Squire, J. P., Olsen, C. S., Cassady, L. D., Ballenger, M. G., Carter, M. D., Ilin, A. V., Glover, T. W., McCaskill, G. E., Chang Díaz, F. R., and Bering, E. a., "Improved Efficiency and Throttling Range of the VX-200 Magnetoplasma Thruster," *Journal of Propulsion and Power*, Vol. 30, No. 1, 2014, pp. 123–132.

[12] Petro, E. M. and Sedwick, R. J., "Effects of Water Vapor Propellant on Helicon Thruster Peformance," *52nd AIAA/SAE/ASEE Joint Propulsion Conference*, AIAA 2016-4735, Salt Lake City, Utah, 2016.

[13] SuperPower Inc., "2G HTS Coils," *http://www.superpower-inc.com/system/files/SP_Coil+Fact+Sheet_2014_v1.pdf*, 2014, pp. Accessed on Sept. 1, 2017.

[14] Hazelton, D. W., "2G HTS Wire Development at SuperPower," *https://nationalmaglab.org/images/magnet_development/asc/searchable_docs/asc_resources/coated_conductors/2016/io_14_hazelton.pdf*, 2016, pp. Accessed on Sept. 1, 2017.

[15] AMSC, "Effects of Temperature and Magnetic Field on Amperium ® Wire Performance," *http://www.amsc.com/library/AMPIcBT_AN_A4_0112.pdf*, 2012, pp. Accessed on Sept. 1, 2017.

[16] Chabert, P. and Braithwaite, N., *Physics of Radio-Frequency Plasmas*, Cambirdge University Press, Cambridge, U.K., 2011, p. 131.

[17] Zhou, D., Ohmi, K., Oide, K., Ã, T. M., Rudenko, T. S., Funaki, I., Shamrai, K. P., and Nakamura, T., "One Dimensional Modeling of Radio Frequency Electric Field Penetration into Magnetized Plasmas," *Japanese Journal of Applied Physics*, Vol. 51, No. 9R, 2012, pp. 096021.

[18] Birdsall, C. K. and Langdon, A., *Plasma Physics Via Computer Simulation*, McGraw-Hill, Inc., New York, NY, 1985.